Journal of Fluids and Structures 18 (2003) 119–130

JOURNAL OF FLUIDS AND STRUCTURES

www.elsevier.nl/locate/jnlabr/yjfls

PIV measurements of near wake behind a U-grooved cylinder

H.-C. Lim[a], S.-J. Lee[b,*]

[a] School of Environmental Engineering, Pohang University of Science and Technology, Pohang 790-784, South Korea
[b] Department of Mechanical Engineering, Pohang University of Science and Technology, Pohang 790-784, South Korea

Received 26 September 2002; accepted 3 July 2003

Abstract

The flow structure around a circular cylinder with U-grooved surfaces has been investigated experimentally. The results were compared with that of a smooth cylinder having the same diameter. Drag force and turbulence statistics of wake behind each cylinder were measured for Reynolds numbers based on the cylinder diameter ($D = 60$ mm) in the range $Re_D = 8 \times 10^3 - 1.4 \times 10^5$. At $Re_D = 1.4 \times 10^5$, the U-type grooves reduce the drag coefficient acting on the cylinder by 18.6%, compared with that of smooth cylinder. The flow characteristics of wake behind the U-grooved cylinder have been analyzed using two kinds of particle image velocimetry (PIV) velocity measurement techniques, cinematic PIV and high-resolution PIV. Consecutive instantaneous velocity fields were measured using the cinematic PIV technique at time interval of 5 ms, corresponding to about 1% of the vortex shedding frequency of the wake. The instantaneous velocity fields measured with the high-resolution PIV technique were ensemble-averaged to get the spatial distributions of turbulent statistics including turbulent intensities and turbulent kinetic energy. For the case of smooth cylinder, large-scale vortices formed behind the cylinder maintain round shape and do not spread out noticeably in the near wake. However, for the case of U-grooved cylinder, the vortices are largely distorted and spread out significantly as they go downstream. The longitudinal grooves seem to shift the location of spanwise vortices toward the cylinder, reducing the vortex formation region, compared with the smooth cylinder. The sharp peaks of longitudinal U-shaped grooves also suppress the formation of large-scale secondary streamwise vortices. The secondary vortices are broken into smaller eddies, reducing turbulent kinetic energy in the near-wake region.

1. Introduction

During the last few decades, the effective control of flow around bluff bodies has been an important theme in many engineering applications. In particular, recent advances in microfabrication and active feedback flow control techniques make it possible to employ artificial manipulations for drag reduction. Since drag reduction is closely related to energy saving, extensive efforts have been made to reduce drag acting on moving bluff bodies.

Passive flow control methods require no external energy input. They control the flow structure by changing the surface configuration or attaching additive devices such as riblets or LEBUs (Large Eddy Breakup Devices) to a body tested (Gad-el-Hak, 1989). Bandyopadhyay (1986) reviewed various flow control techniques for drag reduction and investigated turbulent boundary layers over longitudinal grooved surfaces. Many researchers have studied the effect of surface modifications on turbulent boundary layers (Walsh, 1983; Bechert and Bartenwerfer, 1989; Choi, 1989). Recently, Lee and Lee (2001) measured the near-wall turbulent structure over semi-circular (U-shaped) grooves with tip-to-tip spacing $s = 3$ mm using a particle image velocimetry (PIV) velocity field measurement technique. They found how the grooved surface reduces the drag acting on the surface. As an extension of this study to a bluff body, we investigated the flow around a U-grooved cylinder having the same groove spacing of $s = 3$ mm in the present study.

*Corresponding author. Tel.: +82-54-279-2169; fax: +82-54-279-3199.
E-mail address: sjlee@postech.ac.kr (S.-J. Lee).

0889-9746/$ - see front matter © 2003 Elsevier Ltd. All rights reserved.
doi:10.1016/S0889-9746(03)00086-0

The longitudinal grooves have been used as an effective flow control device for drag reduction and heat transfer enhancement (Gad-el-Hak, 1989). The performance of grooved surfaces applied on bluff bodies has been known to depend largely on the surface configuration of adapted grooves. Achenbach (1971) and Guven et al. (1980) mentioned that surface roughness on a circular cylinder influences the vortex shedding, drag coefficient and heat-transfer characteristics. Ko et al. (1987) and Leung and Ko (1991) investigated the effect of a V-groove configuration on the reduction of drag on a circular cylinders by measuring the surface pressure and Strouhal number variations. However, the V-grooved and smooth cylinders showed nearly the same drag coefficient in the Reynolds number range from 2×10^4 to 1.6×10^5. Recently, Lim and Lee (2002) investigated the flow around circular cylinders with U- and V-shaped grooved surfaces by measuring the drag force, mean velocity and turbulence statistics of the wake. The U-shaped grooves were found to be more effective in drag reduction, compared with the V-shaped grooves. However, the detailed drag reduction mechanism and the modified three-dimensional (3-D) flow structure around the U-grooved cylinders have not been fully understood yet.

Zhang et al. (1995) observed the transition in the cylinder wake with predominant spanwise wavelengths of $\lambda = 1-4D$ at small Reynolds numbers of $\mathrm{Re} = 150-250$. Lin et al. (1995) investigated 3-D flow pattern and spatial correlation of instantaneous streamwise vorticity behind a cylinder using a PIV velocity field measurement technique. Gerrard (1966) and Wei and Smith (1986) mentioned that, at high Reynolds number larger than $\mathrm{Re} = 10^3$, the near-wake behind a bluff body has a complicated flow structure, resulting from the onset of small-scale vortical structures due to flow instability of the shear layer.

Though the effective flow control for drag reduction has been very important for practical engineering applications, the wake structure behind a bluff body wake modified by longitudinal grooves has not been fully understood yet. From an aerodynamic point of view, it is important to investigate the modified wake structure for effective control of flow around the cylinder.

The main objective of this study is to investigate the effect of U-grooves on drag reduction and flow structure in the near-wake region. The velocity fields of near-wake behind a circular cylinder were measured using PIV velocity field measurement techniques.

2. Experimental apparatus and method

2.1. Experimental setup

Two circular cylinders of the same diameter ($D = 60$ mm) with different surface configurations were tested in this study. One cylinder has a smooth surface and the other has longitudinal grooves of semi-circular (U-grooved) shape. The cylinder models were made of Teflon pipe of length $L = 600$ mm. Walsh (1983) suggested the riblet surface with a sharp peak and large radius of curvature as an optimum shape for drag reduction. The U-grooved cylinder with tip-to-tip spacing of $s = 3$ mm was tested in present study. The schematic diagram of U-grooved cylinder and coordinate system used in this study are shown in Fig. 1.

Study on the flow around the grooved and smooth cylinders was carried out in a closed-return type subsonic wind tunnel with a test-section of 0.72 m wide, 0.6 m high and 6 m long. The free-stream turbulence intensity in the test-section was less than 0.08% at $U_0 = 10$ m/s. The experiments were performed with varying Reynolds number based on the cylinder diameter D in the range of $\mathrm{Re}_D = 8000-140\,000$.

The formulas of Allen and Vincenti (1944) were employed to correct the flow velocity and pressure data for blockage and wall interference effects due to presence of the experimental models in the tunnel. Two rectangular end-plates of 2 mm thickness were installed at the ends of the cylinder to minimize the boundary layer developing along the tunnel sidewalls and to maintain two-dimensional flow characteristics (Stansby, 1974).

Fig. 2 shows the schematic diagram of experimental setup for drag, velocity and surface pressure measurements. For measuring the drag force acting on the cylinder, a set of dummy cylinder and load-cell was attached at both ends of the cylinder model. In addition, a concentric hollow dummy cylinder of about 5 cm long and rectangular end-plates were installed at both sidewalls of the wind tunnel test-section to avoid the effect of tunnel wall interference on the cylinder. The aerodynamic forces were measured using two 3-component load-cells (Nissho LMC-3502) whose nonlinearity is less than 0.5% of full scale (5 kg). One load-cell measures the aerodynamic force, the other is a dummy for balancing. The load-cell was coupled with a DC strain amplifier (DSA-100) connected to a high-precision A/D converter (DT2838). The drag coefficient based on the effective frontal area (A) of the cylinder model was defined as follows:

$$C_D = Drag/(\rho U_0^2 A/2). \tag{1}$$

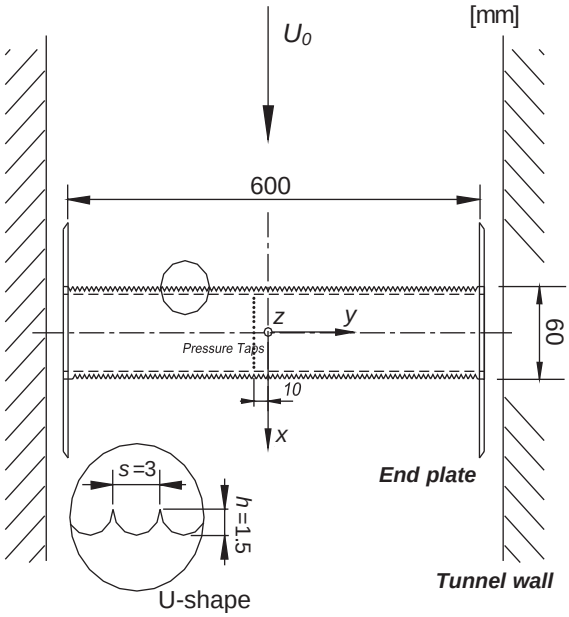

Fig. 1. Top view of experimental setup and coordinate system (units: mm).

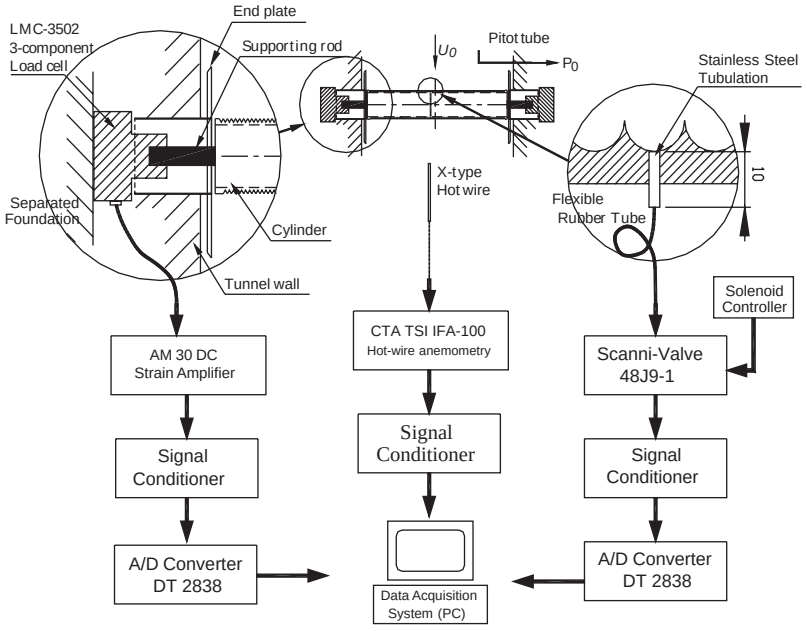

Fig. 2. Schematic diagrams of the drag, velocity and pressure measurement system.

The turbulence characteristics of the flow behind the cylinder were measured using an I-type hot-wire probe (DANTEC 55P11) connected to a constant temperature hot-wire anemometer (TSI IFA 100) and DT2838 A/D converter. The hot-wire probe was traversed to measuring positions using a 3-D traverse with an accuracy of 0.01 mm. During the experiments, the temperature variation in the wind tunnel test-section was maintained to be less than 0.5°C. To investigate the vortex structure in the near wake, the shedding frequency of velocity signals measured by a hot-wire probe at a point ($x/D = 2$, $y/D = 0.5$) was spectrally analyzed. At each measurement point, 8196 velocity data were acquired at 2000 samples/s, after low-pass filtering at 800 Hz.

To measure surface pressure distributions, 36 taps were installed on the valley bottom of longitudinal grooves along the peripheral of the cylinder at $y = -10$ mm cross-section as shown in Figs. 1 and 2. The inner diameter of the stainless-steel pressure taps was 0.8 mm. The pressure taps were connected to a micromanometer (FCO-19) and the analog pressure signals were digitized using a high-precision A/D converter (DT-2838). At each measurement point, 16384 pressure data were acquired at a sampling rate of 500 Hz after low-pass filtering at 200 Hz. Time delay of a few seconds was given to recover pressure fluctuations after each channel scanning.

The pressure difference between the surface pressure p on the cylinder surface and the static pressure p_0 measured at the location ($x/D = -8$, $y/D = 3$, $z/D = 2$) was nondimensionalized by the dynamic pressure $0.5\rho U_0^2$ to give the pressure coefficient, C_p, in the following form:

$$C_p = 2(p - p_0)/\rho U_0^2. \tag{2}$$

2.2. Cinematic PIV

Consecutive instantaneous velocity fields behind the smooth and U-grooved cylinders were measured using the cinematic PIV technique for investigating the time evolution of spanwise vorticity and formation of large-scale vortices. Silver-coated small particles with an average diameter of 2–3 μm were seeded as tracer particles in a circulating water channel having a test-section of width × height × length = 0.3 m × 0.25 m × 1.2 m. The cylinder models were mounted horizontally inside the water channel without end plates. Due to smallness of the test-section of the water channel, the blockage ratio of the cylinder models was about 25%, much higher than that (8%) for the wind tunnel tests. The PIV velocity field measurements were carried out at two planes; One is the longitudinal plane for plane view and the other is the sagittal plane for end view at $x/D = 1.5$ downstream location as shown in Fig. 3. The measurement planes were illuminated with a thin light sheet of 4 W Argon-ion laser. The high-speed CCD camera (SpeedCam$^+$) can capture digital flow images at the frame rate of 1000 fps (frame per second) with full resolution of 512×512 pixels.

In order to see cinematically the evolution of flow structure behind the cylinders, particle images were captured at the time interval of 5 ms, corresponding to about 1% of the characteristic period of large-scale vortex formation. Five hundreds instantaneous velocity fields were obtained using a cross-correlation 2-frame PIV method.

The wake behind the U-grooved cylinder at a Reynolds number of 7×10^4 was compared with those for the smooth cylinder. The field of view was $120 \times 120\,\text{mm}^2$ in physical size. The interrogation window size was 32×32 pixels with a 50% overlap, giving 961 (31×31) velocity vectors in each instantaneous velocity field.

2.3. High-resolution PIV technique

Instantaneous velocity fields of the wake behind the grooved cylinder were also measured using the high-resolution 2-frame PIV system. The PIV system consists of a two-head Nd:Yag laser, a 2K × 2K Kodak CCD camera, a frame grabber, a delay generator and an IBM PC as shown in Fig. 4. The maximum energy output of the pulse laser is larger than 25 mJ per pulse. Since the two-head Nd:Yag laser pulse has a very short pulse width of about 7 ns, the highly turbulent eddy motions can be captured in a clear image. A delay generator was employed to synchronize the Nd:Yag laser and CCD camera. The time interval Δt between two consecutive frames was controlled using the delay generator. During the time interval Δt, some particles move in and move out of the laser light. Therefore, the time interval Δt and the thickness of the laser light sheet were carefully determined in the consideration of maximum particle displacement in the interrogation window. The laser light sheet of about 4 mm was used in this experiment. Details of the 2-frame PIV velocity field measurement system and its accuracy are described in Lee (2001).

The mean velocity field was obtained by ensemble-averaging 500 instantaneous velocity fields. All fluctuating velocity fields subtracted the mean velocity field from the instantaneous velocity fields were statistically averaged to get spatial distribution of turbulence statistics. The vorticity was calculated using the following discretization equation:

$$\begin{aligned}\omega_x &= \frac{1}{2}\left(\frac{\partial W}{\partial y} - \frac{\partial V}{\partial z}\right)\\ &\approx \frac{1}{2}\left(\frac{2W_{i+2,j} + W_{i+1,j} - W_{i-1,j} - 2W_{i-2,j}}{10\Delta y} - \frac{2V_{i,j+2} + V_{i,j+1} - V_{i,j-1} - 2V_{i,j-2}}{10\Delta z}\right).\end{aligned} \tag{3}$$

The turbulence kinetic energy k was calculated using the following two-dimensional approximation:

$$\bar{u}^2 \approx \tfrac{1}{2}(\bar{v}^2 + \bar{w}^2), \quad k = \tfrac{1}{2}\rho(\bar{u}^2 + \bar{v}^2 + \bar{w}^2) \approx \tfrac{3}{4}\rho(\bar{v}^2 + \bar{w}^2). \tag{4}$$

Due to the assumption of an isotropic turbulent structure, the real turbulence kinetic energy will be a little different from the present results in the regions of nonisotropic turbulent structure.

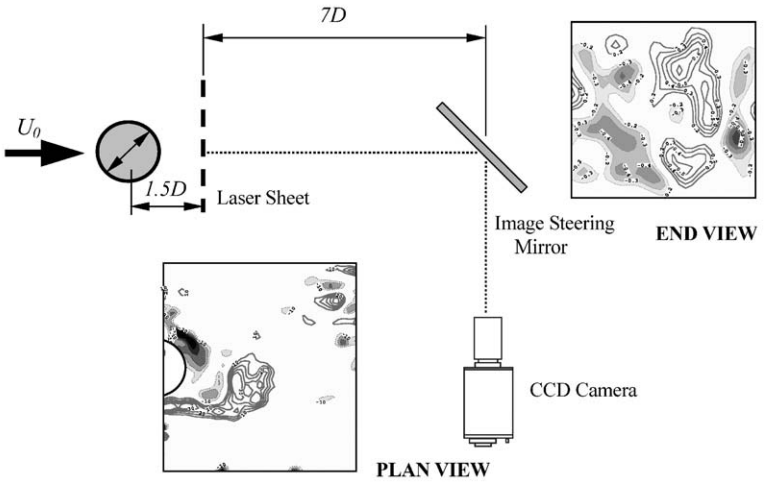

Fig. 3. Measurement planes for PIV velocity field measurements in a circulating water channel.

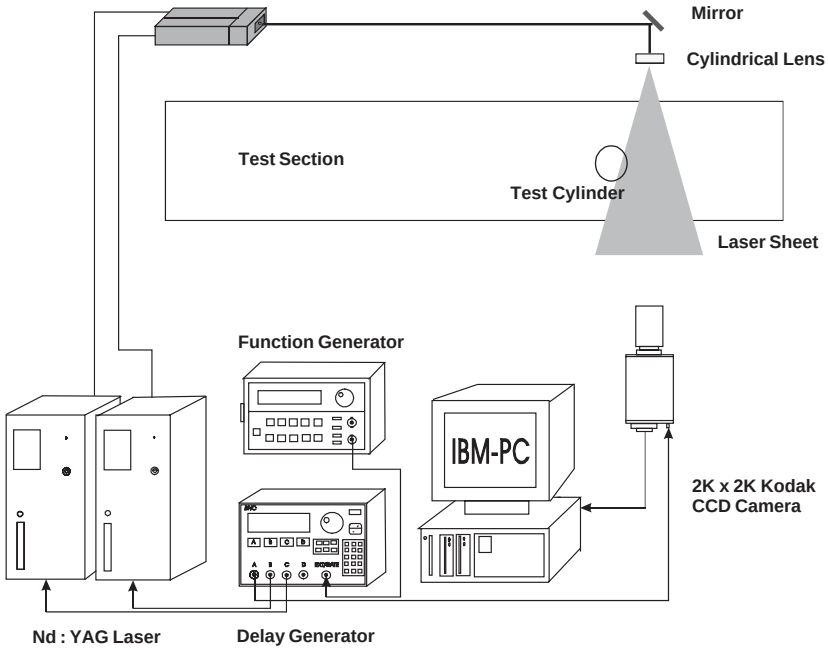

Fig. 4. Schematic diagram of experimental setup for high-resolution PIV measurements.

3. Results and discussion

3.1. Drag force

Fig. 5 shows the variation of drag coefficient with respect to Reynolds number. The values of the drag coefficient were corrected by applying the method suggested by Allen and Vincenti (1944) with respect to blockage ratio. The results of Wieselsberger (1923) are compared with the present results. The pressure drag coefficient C_p represented as solid marks was obtained by integrating the pressure data around the cylinder surface. Error bars indicate the error bound encountered in obtaining the drag coefficients with 95% confidence.

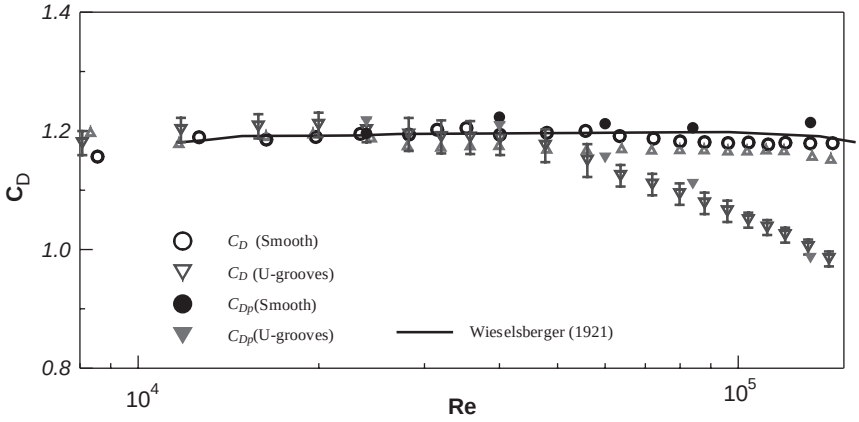

Fig. 5. Variation of drag coefficient with respect to Reynolds number.

The drag coefficient for the smooth cylinder is nearly constant and has an average value of 1.2. It agrees well with those of previous results measured in the ranges of $10^4 < \mathrm{Re}_D < 10^5$. In addition, the pressure drag coefficients CD_p are nearly well-matched with the total drag coefficients at the same condition within the subcritical regime. The pressure drag for the U-grooved cylinder shows a similar tendency with the total drag coefficient variation in the range of Reynolds numbers tested in this study. The U-grooved cylinder has nearly the same values of drag coefficient as the smooth cylinder up to the Reynolds number of 4×10^4. Thereafter, the drag coefficient of the U-grooved cylinder decreases substantially. The drag coefficient of the U-groove circular cylinder is reduced about 18.6% at the Reynolds number of $\mathrm{Re}_D = 1.4 \times 10^5$.

Ko et al. (1987) investigated flow around a V-grooved cylinder in the Reynolds number range from 2×10^4 to 1.6×10^5. They found that the transitions from subcritical to critical and from critical to supercritical flow regimes for the V-grooved cylinder occur at lower Reynolds numbers, compared with the smooth cylinder. In this study, the flow regime does not reach the critical Reynolds number; however, the drag coefficients for the smooth cylinder show a similar result with respect to Reynolds number.

3.2. Wake flow characteristics

The power spectral density (PSD) distributions measured at a downstream location $x/D = 2$, $y/D = 0.5$ are shown in Fig. 6 at four different Reynolds numbers: Re_D =24 000, 40 000, 56 000 and 96 000. Here, $S(f)$ and $S(f_0)$ represent the PSD value at frequency f and at the dominant shedding frequency f_0, respectively. The vortex shedding frequency f is expressed as a nondimensional parameter, the Strouhal number ($\mathrm{St} = fD/U_0$). A clear and distinct PSD peak indicates the existence of a dominant vortex structure caused by regular vortex shedding.

As the Reynolds number increases, the PSD peak becomes distinctive and the Strouhal number corresponding to PSD peak location approaches to a value of $\mathrm{St} = 0.18$ for the smooth cylinder. However, for the case of U-grooved cylinder, the vortex shedding frequency increases gradually with increasing Reynolds number. In addition, the PSD peak for the smooth cylinder has relatively small values of around 0.1–0.3. On the other hand, the peak values for the grooved cylinder increase gradually with increasing Reynolds number. These results indicate that U-grooves on the cylinder surface effectively suppress the formation of large-scale vortices.

3.3. Surface pressure

The effect of Reynolds number on the pressure distribution measured at midsection of three cylinders are shown in Fig. 7. For comparison, the results of Roshko (1954) at $\mathrm{Re} = 14\,500$ and Fage and Falkner (1931) at $\mathrm{Re} = 1.1 \times 10^5$ for a smooth cylinder were included.

In the subcritical regime less than the critical Reynolds number $\mathrm{Re}_c = 3 \times 10^5$, the boundary layer separates in a laminar state at about 80° from the forward stagnation point, and the early separation results in a drag coefficient of about 1.2. The pressure coefficients for the smooth cylinder agree well with those of Roshko (1954) and Fage and Falkner (1931). For the smooth cylinder, the surface pressure distribution does not show any remarkable variations in the range of $2 \times 10^4 < \mathrm{Re}_D < 1.3 \times 10^5$.

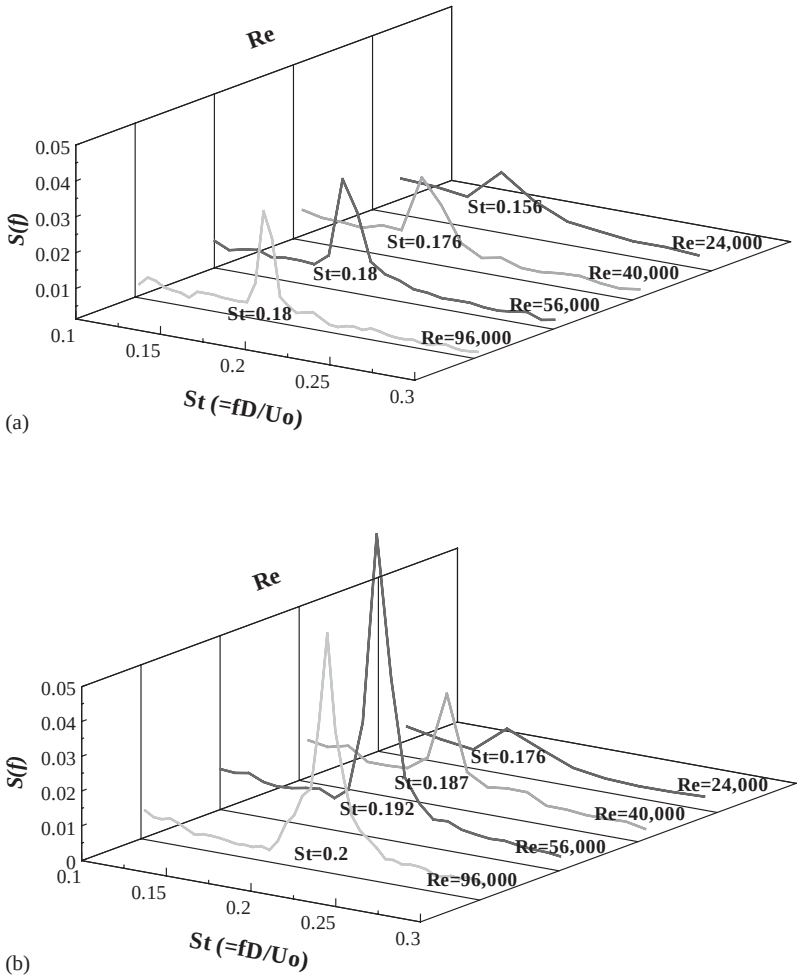

Fig. 6. Comparison of nondimensional PSD distribution: (a) smooth cylinder and (b) U-grooved cylinder.

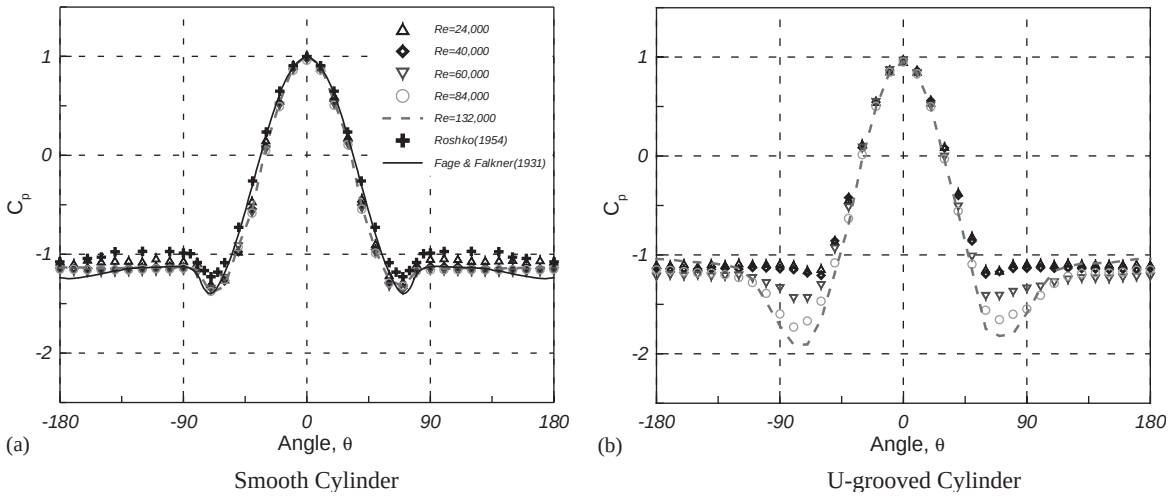

Fig. 7. Comparison of surface pressure distributions (Uncertainty in $C_p < \pm 2\%$).

The pressure distributions on the U-grooved cylinder surface (Fig. 7(b)) are quite different from those of the smooth cylinder, even though the flow is within the subcritical regime. The surface pressure distributions show large variations around the separation region. As the Reynolds number increases, the separation point shifts downstream and the local minimum surface pressure decreases. This may be attributed to the fact that the longitudinal grooves on the cylinder surface enhance the boundary layer transition from laminar to turbulent flow. In addition, the base pressure at Reynolds number $Re_D = 1.32 \times 10^5$ is higher than that at Reynolds number $Re_D = 2.4 \times 10^4$. From these results, it can be conjectured that the U-grooves cause a substantial decrease of drag coefficient at high Reynolds numbers, compared with the smooth cylinder.

3.4. Temporal evolution of near-wake structure

The instantaneous velocity fields of near-wake behind the smooth and U-grooved cylinders were measured sequentially using the cinematic PIV technique at a time interval of 5 ms. Contour plots of spanwise vorticity ω_y measured in the longitudinal plane are shown in Fig. 8. Contours of positive vorticity are represented as solid lines and negative vorticity values are depicted in gray tones. Large-scale vortices are shed from the lower side of the cylinder and

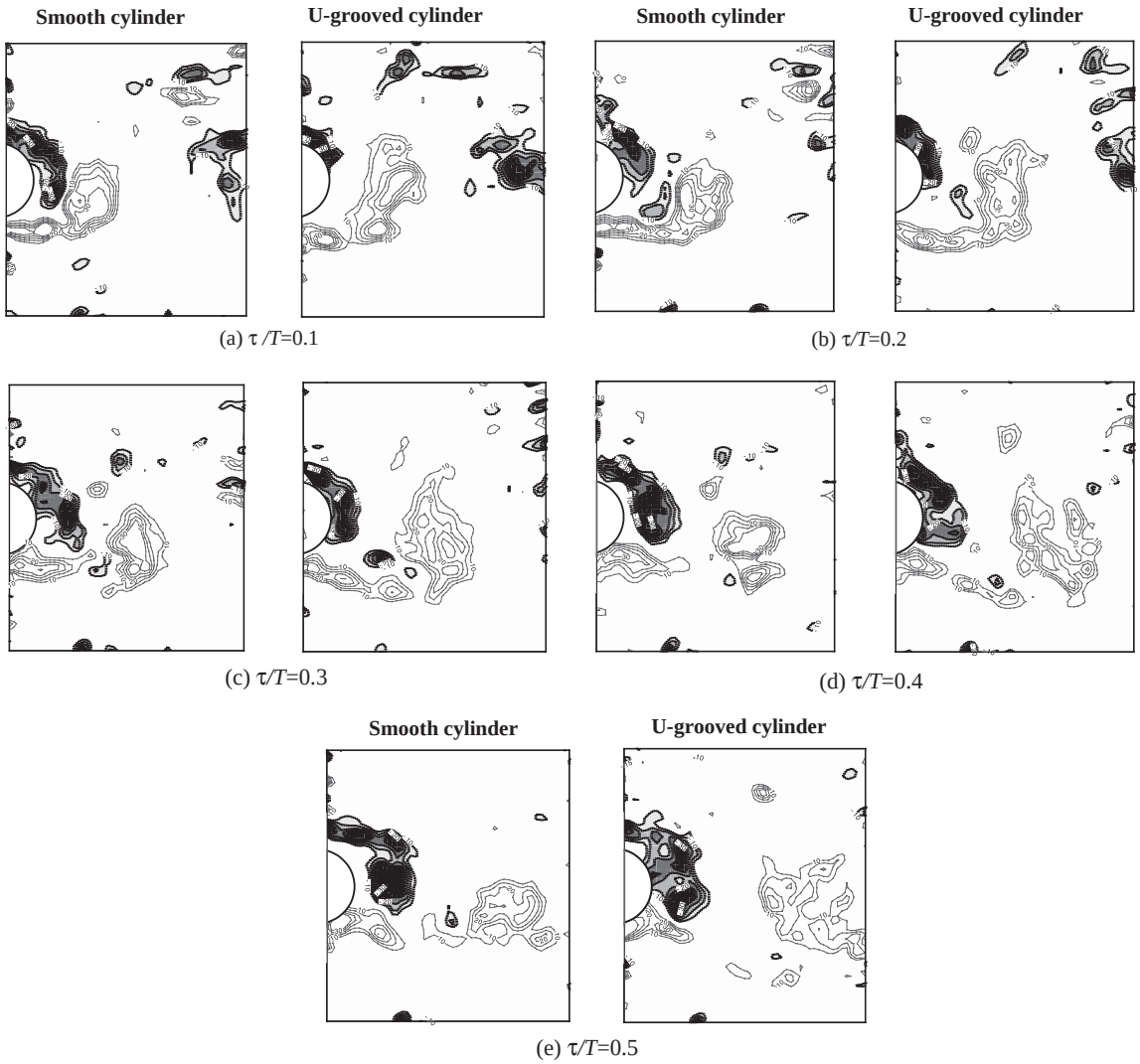

Fig. 8. Variation of instantaneous vorticity field at Re = 70 000 (Left: smooth cylinder, Right: U-grooved cylinder) (a) $\tau/T = 0.1$; (b) $\tau/T = 0.2$; (c) $\tau/T = 0.3$; (d) $\tau/T = 0.4$; and (e) $\tau/T = 0.5$.

move downstream. For the case of a smooth cylinder represented on the left side, a large-scale vortex is formed just behind the cylinder and maintains its round shape in the near-wake region and does not spread out noticeably with the lapse of time. However, the vortices formed behind the U-grooved cylinder are largely distorted and spread out significantly with as they go downstream.

The vortices formed behind the upper side of U-grooved cylinder are attached on the cylinder even at the $\tau = 0.5\,\mathrm{T}$. However, the vortices behind smooth cylinder start to separate from the cylinder at $\tau = 0.3\,\mathrm{T}$ and their centers are located slightly downstream at the same elapse of time.

3.5. Ensemble-averaged mean velocity field

The spatial distributions of vorticity and turbulence kinetic energy were obtained by ensemble averaging 500 instantaneous velocity fields for both smooth and U-grooved cylinders. Fig. 9 shows the flow speed distributions in xz plane measured at the mid-section of each cylinder. In order to see the intrinsic flow structure, streamlines that are everywhere tangent to the velocity vectors are also represented together. The flow speed behind the U-grooved cylinder has nearly the same values in the near-wake region as those of the smooth cylinder. On the other hand, the streamlines clearly show that the size of vortex formation region for the U-grooved cylinder is about $x/D = 1.1$, smaller than that ($x/D = 1.2$) of the smooth cylinder.

The contour plots of spanwise vorticity (ω_y) in xz plane for both smooth and U-grooved cylinders are shown in Fig. 10. The spanwise vorticity $+\omega_y$ and $-\omega_y$ has large values in both side edges of the cylinder due to formation of

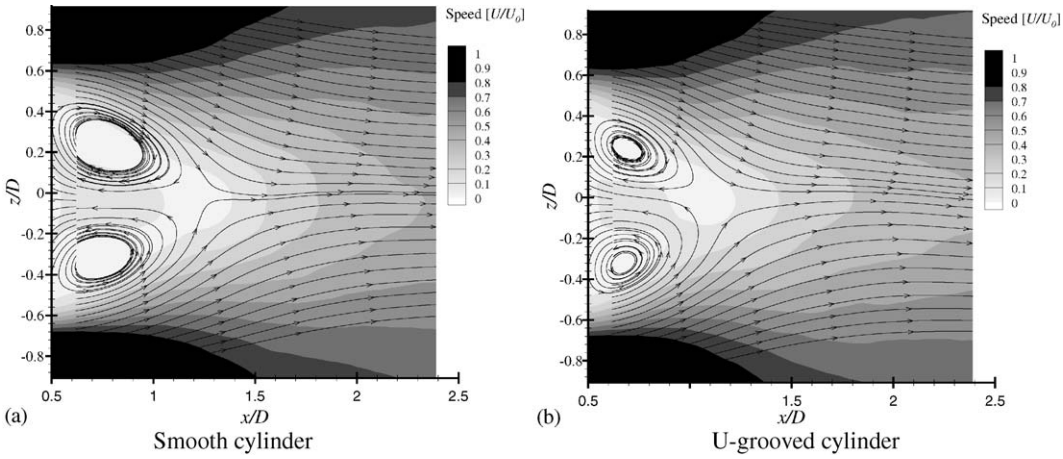

Fig. 9. Spatial distributions of flow speed and streamlines in longitudinal (xz) plane.

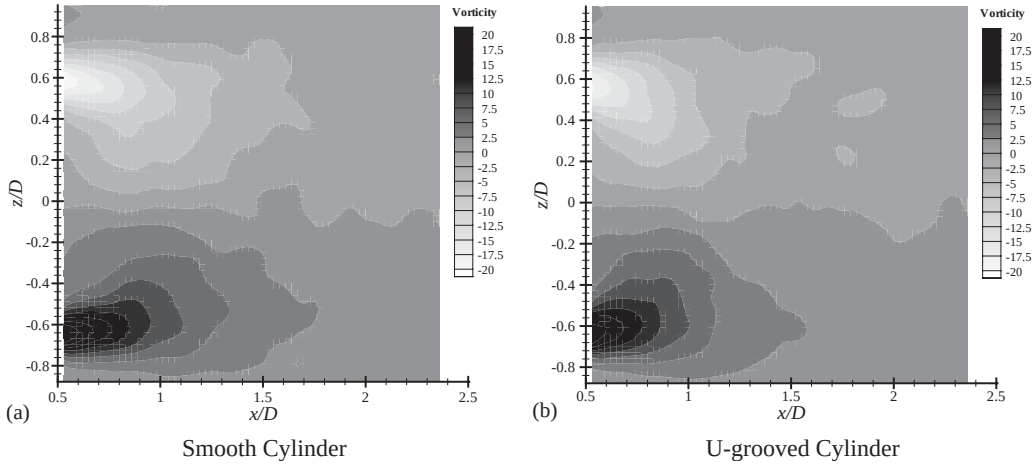

Fig. 10. Contour plots of spanwise vorticity (ω_y) in longitudinal (xz) plane.

large-scale vortices. The smooth cylinder shows slightly elongated vorticity contours. However, the U-grooved cylinder shows more or less circular contours, and the centers of vortices are shifted back toward the cylinder. These vorticity contours agree well with the previous results discussed so far, especially the shorter vortex formation region of the U-grooved cylinder.

Fig. 11 compares the ensemble-averaged turbulence kinetic energy distribution measured at the sagittal (yz) plane of $x/D = 1.5$. On the average, the smooth cylinder has large turbulence kinetic energy and regions of large and small kinetic energy exist together. However, the U-grooved cylinder seems to reduce the turbulence kinetic energy in the near wake and does not have large values except in the upper-left small area. This may be attributed to the fact that formation of secondary vortices is suppressed in the region behind the U-grooved cylinder. The secondary vortices are broken into smaller eddies due to sharp peaks of the longitudinal U-shaped grooves. This can be conjectured from the PSD results in which the U-grooved cylinder shows higher shedding frequency, compared with the smooth cylinder.

Fig. 12 shows the spatial distributions of vertical velocity component (W) in the cross-sectional yz plane at $x/D = 1.5$. The cross-sectional views clearly reveal the lateral vortical structure induced by the three-dimensional deformation of the secondary vortices. The large-scale vortices shed from both sides of each cylinder cross the wake-center axis at the end of vortex formation region. The vertical velocity (W) has positive and negative values in the lower and upper wake region, indicating the flow moving toward the wake center region. The vertical velocity component shows a more or less

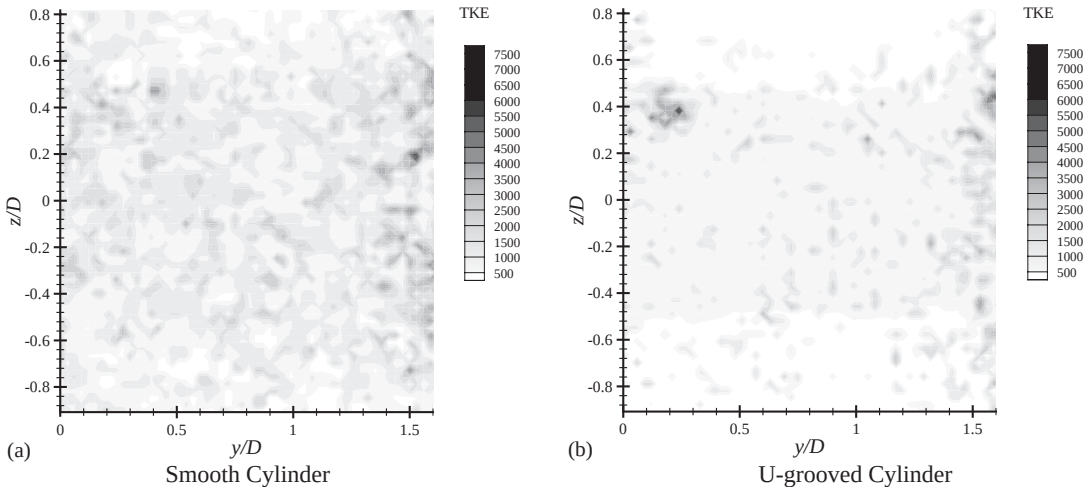

Fig. 11. Turbulence kinetic energy distribution at sagittal (yz) plane of $x/D = 1.5$.

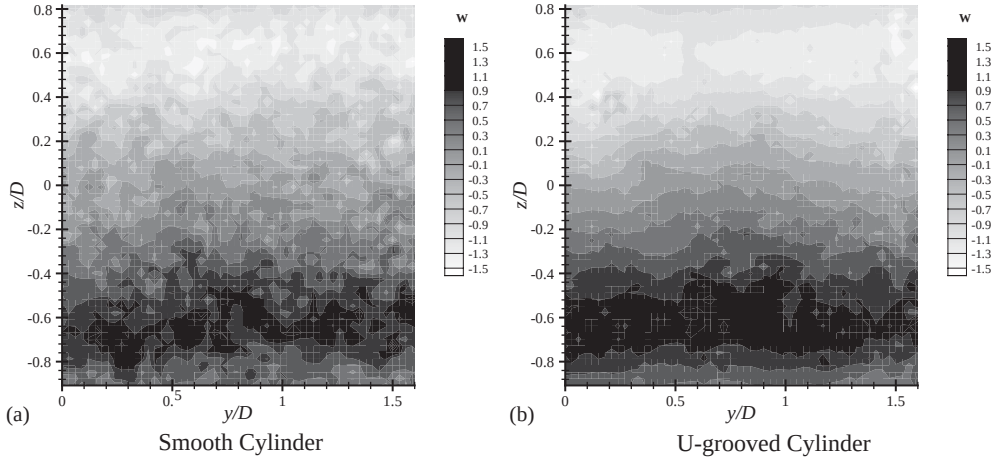

Fig. 12. Spatial distribution of vertical velocity component (W) at $x/D = 1.5$.

irregular and random distribution in the region behind the smooth cylinder. On the contrary, for the case of U-grooved cylinder, the grooves on the cylinder surface make a nearly uniform distribution of vertical velocity along the spanwise direction. This seems to be related with the suppression of lateral movement of the flow due to the longitudinal U-shaped grooves. Fig. 13 shows the contour plots of the normalized flow speed ($\sqrt{V^2 + W^2}/U_0$). As shown in the Fig. 12, the smooth cylinder shows relatively large spatial variation of flow speed. However, the U-grooved cylinder shows nearly uniform lateral distribution and has small speed in the wake center.

The center locations of longitudinal vortices were derived by finding the positions of maximum vorticity value larger than a preset threshold value. The results obtained from 500 consecutive instantaneous velocity fields are shown in Fig. 14. In order to compare the vorticity center distributions, the same criteria on the threshold values were applied for both cases. For the case of a smooth cylinder (Fig. 14(a)), most vorticity centers are uniformly distributed in the sagittal (yz) plane behind the cylinder. In addition, the smooth cylinder has larger number of vorticity centers, compared with the U-grooved cylinder. However, the total number of streamwise vortices ω_x for the case of the U-grooved cylinder is relatively small, especially in the wake center region. It can be conjectured that the longitudinal grooves suppress the formation of large-scale secondary vortices and the longitudinal vortices dissipate rapidly and propagate widely leading to an irregular distribution. These results confirm the results discussed in Figs. 11 and 12. These spatial distributions of

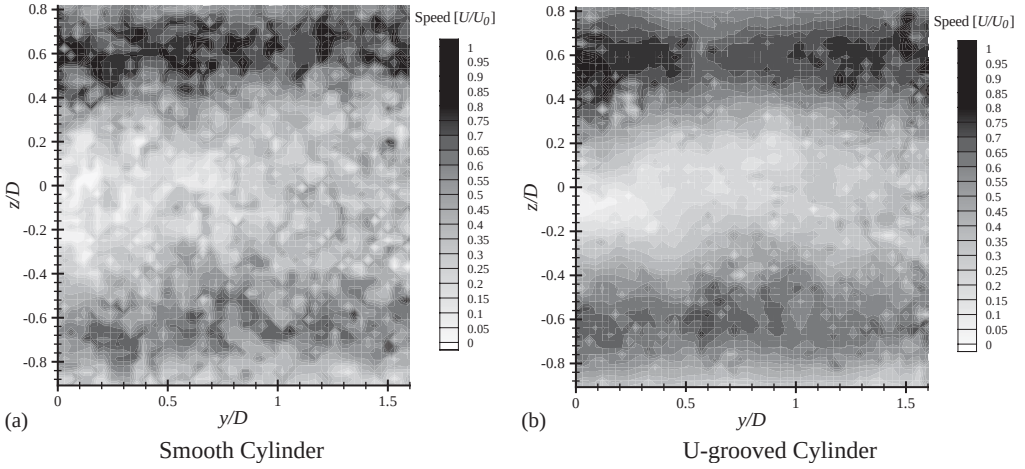

Fig. 13. Contour plots of normalized flow speed $\left(\sqrt{V^2 + W^2}/U_0\right)$.

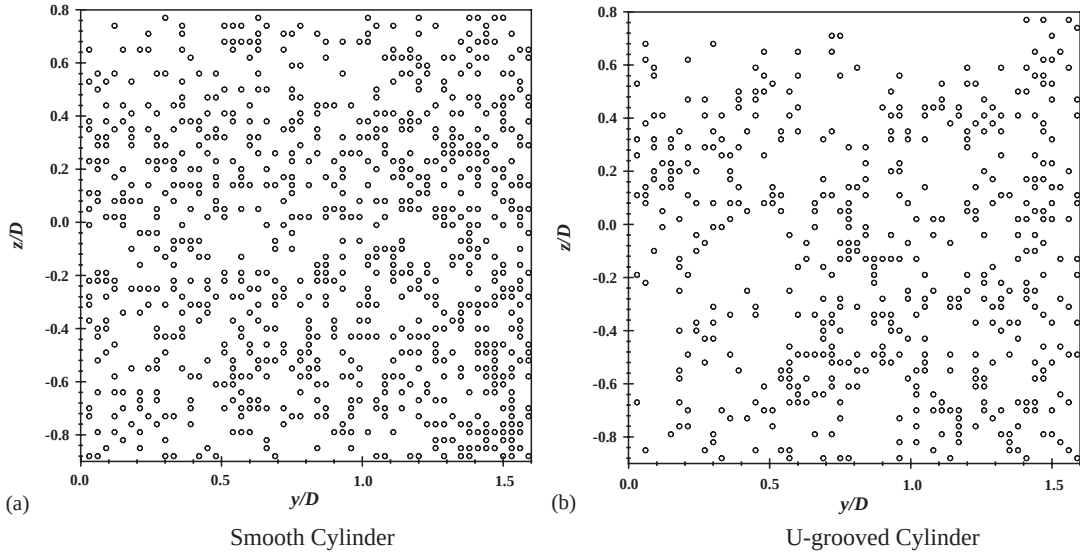

Fig. 14. Comparison of center locations of streamwise vortices derived from 500 consecutive instantaneous velocity fields.

kinetic energy and vortices in the sagittal plane show clearly the difference of the near-wake structure between the smooth and U-grooved cylinders.

4. Conclusion

The flow structure of wake behind a circular cylinder with longitudinal U-grooves has been investigated experimentally using PIV velocity field measurement techniques. The U-grooved cylinder reduces the drag coefficient by about 18.6%, compared with the smooth cylinder at $Re_D = 1.4 \times 10^5$. The drag reduction of the U-grooved cylinder increases with increasing Reynolds number.

The vortex formation region behind U-grooved cylinder is smaller than for the smooth cylinder. The longitudinal grooves seem to reduce the size of spanwise vortices and shift their location toward the cylinder. The sharp peaks of longitudinal U-shaped grooves also suppress the formation of large-scale secondary streamwise vortices. The secondary vortices are broken into smaller eddies, reducing the turbulence kinetic energy in the near-wake region.

Acknowledgements

This work was supported by NRL (National Research Laboratory) program sponsored by Ministry of Science and Technology (MOST) of Korea.

References

Achenbach, E., 1971. Influence of surface roughness on the crossflow around a circular cylinder. Journal of Fluid Mechanics 46, 321–335.

Allen, H.J., Vincenti, W.G., 1944. Wall interference in a two-dimensional flow and wind tunnel with consideration of the effect of compressibility. National Advisory Committee for Aeronautics Report 782, Washington, DC.

Bandyopadhyay, P.R., 1986. Review—mean flow in turbulent boundary layers disturbed to alter skin friction. Journal of Fluids Engineering 108, 127–140.

Bechert, D.W., Bartenwerfer, M., 1989. The viscous flow on surfaces with longitudinal ribs. Journal of Fluid Mechanics 206, 105–129.

Choi, K.S., 1989. Near-wall structure of a turbulent boundary layer with riblets. Journal of Fluid Mechanics 208, 417–458.

Fage, A., Falkner, V.M., 1931. The flow around a circular cylinder. Aeronautical Research Council Reports and Memoranda 1369, London.

Gad-el-Hak, M., 1989. Flow control. Applied Mechanics Reviews 42, 261–293.

Gerrard, J.H., 1966. The mechanics of the formation region of vortices behind bluff bodies. Journal of Fluid Mechanics 25, 401–413.

Guven, O., Farell, C., Patel, V.C., 1980. Surface roughness effects on the mean flow past circular cylinders. Journal of Fluid Mechanics 98, 673–701.

Ko, N.W.M., Leung, Y.C., Chen, J.J.J., 1987. Flow past V-groove circular cylinder. American Institute of Aeronautics and Astronautics Journal 25, 806–811.

Lee, S.J., 2001. PIV/PTV velocity field measurement technique—theory and practice. PIV '2001 Lecture Note, POSTECH.

Lee, S.J., Lee, S.H., 2001. Flow field analysis of turbulent boundary layer over a riblet surface. Experiments in Fluids 30, 231–246.

Leung, Y.C., Ko, N.W.M., 1991. Near wall characteristics of flow over grooved circular cylinder. Experiments in Fluids 10, 322–332.

Lim, H.C., Lee, S.J., 2002. Flow control of circular cylinders with riblet surfaces. American Institute of Aeronautics and Astronautics Journal 40, 1631–1642.

Lin, J.C., Vorobieff, P., Rockwell, D., 1995. Three-dimensional patterns of streamwise vorticity in the turbulent near-wake of a cylinder. Journal of Fluids and Structures 9, 231.

Roshko, A., 1954. On the development of turbulent wakes from vortex streets. NACA Report 1191.

Stansby, P.K., 1974. The effect of endplates on the base pressure coefficient of a circular cylinder. Aeronautical Journal 78, 36–23133.

Walsh, M.J., 1983. Riblets as a viscous drag reduction technique. American Institute of Aeronautics and Astronautics Journal 21, 485–486.

Wei, T., Smith, C.R., 1986. Secondary vortices in the wake of circular cylinders. Journal of Fluid Mechanics 169, 513–533.

Wieselsberger, C., 1923. Neuere feststellungen uber die gesetze des flussigkeits-und luftwiderstands. Physikalische Zeitschrift 22, 321–328.

Zhang, H.Q., Fey, U., Noack, B.R., Konig, M., Eckelmann, H., 1995. On the transition of the cylinder wake. Physics of Fluids 7, 779–794.